Full length article

Single-step self-compression of ultrashort pulses below 20 fs by all-fiber supercontinuum generation

Francisco Javier Salgado-Remacha [*], Sebastián Jarabo

Universidad de Zaragoza, Departamento de Física Aplicada, Facultad de Ciencias, C/ Pedro Cerbuna 12 50009 Zaragoza Spain

A B S T R A C T

We present an ultrashort-pulsed laser source with time-widths as short as 20 fs at around 1.5 μm. For this purpose, the pulses have been spectrally broadened and temporally compressed by means of supercontinuum generation in a highly nonlinear optical fiber. Inspired by numerical simulations, we have experimentally confirmed that the emission of a resonant dispersive wave is a key indicator for the optimum configuration to achieve maximum temporal compression. No dispersion control stage is needed, which results in the simplicity of the system. An extensive analysis has been made concerning the quality of the pulses obtained, particularly in terms of time-width (at half height and at 1/e height of the maximum) as well as their time-bandwidth product. The complex retrieval of the pulses shows that the smallest temporal width obtained experimentally is 17 fs. A comparison with values found in the literature also shows that our pulses are among the best that can be found with this technology.

1. Introduction

Ultrashort laser pulses, whose widths are below the picosecond, are the basis for the most recent developments in fields such as nonlinear optics or quantum optics. Typically, these pulses are generated by mode-locking lasers in different spectral ranges. In particular, fiber optic ring lasers offer certain advantages, such as mechanical stability and easiness of pulse insertion in fiber optic circuits [1]. Thus, for example, erbium-doped fiber lasers emit pulses in the telecommunications band (around 1.5 μm), with time-widths of a few hundred femtoseconds easily attainable. These light sources make it easy to produce nonlinear effects in fiber optics, among which we highlight supercontinuum generation (SCG) because of its relation to this work [2].

The interest in reducing the duration of these pulses is evident, particularly in the field of ultrafast optics (with pulse durations of femtoseconds and even attoseconds). There are typically (but not only) two strategies to achieve this aim. The first one involves propagating the pulse through air and passing it through a pulse compressor, such as a dual-grating system or ultrafast mirrors to control dispersion [3]. Obviously, the advantage of having the pulse confined in the fiber is lost with this method. In the second strategy, the idea is to keep the pulse always confined in the optical fiber, for which fibers with normal and anomalous dispersion can be combined to compensate the dispersion

and compress the light pulses [4].

As the minimum duration of the pulses is limited by the spectral width of the laser oscillation profile in both strategies, in this paper we propose a third strategy to overcome this restriction, based on keeping the pulse confined and making use simultaneously of the nonlinear effects in the optical fiber. The idea is to spectrally broaden the pulse by generating supercontinuum in a Highly Nonlinear Fiber (HNLF). By maintaining some control over the pulse, it is possible to compress the pulse to durations of a few tens of femtoseconds [1]. This strategy usually involves developing and adjusting a number of different stages, which complicates the experimental setup. The results presented in this work show that it is possible to achieve sub-20 fs pulses in a very simple way, with a reduced number of components in the experimental setup. For this purpose, it is necessary to optimize the HNLF length (which depends on the peak power of the seed pulses) with which the maximum temporal compression can be achieved. Using numerical simulations, we show the features in the spectrum that can indicate the maximum pulse compression.

To evaluate the goodness of our results, we also made a comparison with those reported by other authors who also work in the same line. The main advantage of our system is its simplicity (and at a very low cost), since using only a HNLF sample (without the need to control the dispersion afterwards) we are able to obtain pulses below 20 fs. As we

---

will see below, this result is among the best that can be found in the literature, having also a very simple system.

2. Material and methods

The experimental set-up is based on a supercontinuum source introduced in ref. [5]. The supercontinuum is generated in a HNLF (Yangtze Optical Fibre and Cable Company Ltd., NL-1550-Zero type [6]) of 24 m length. The nominal nonlinear coefficient is 10 $W^{-1} \bullet km^{-1}$ and the Raman gain coefficient is higher than 4.8 $W^{-1}\ km^{-1}$, with the zero dispersion parameter D_λ around 1550 nm, and a dispersion slope lower than 0.020 ps$\bullet$nm$^{-2}\bullet$km^{-1}. This HNLF is seeded with an all-fiber mode-locked pulsed laser, with an Erbium doped Fiber Amplifier (EDFA) inside cavity operating in the C-band with + 20 dBm saturation output power (Highwave, model C20-G20-H-FC/APC-BTO 3.0, labelled as EDFA-C20) and operating with a repetition rate of 1.4MHz. The mode-locking is based on the nonlinear polarization rotation effect, using a Lineal Polarizer (LP) placed between two Polarization Controllers (PC). The output of the laser is post-amplified by a second EDFA with + 26 dBm saturation output power (Manlight, model HWT-EDFA-GM-SC-BO-C26, labelled as EDFA-C26). The EDFA-C26 allows us to control the input power in the HNLF. A great effort has been made to optimize the pulses produced by this laser source for the generation of super-continuum, as we will explain later. In this work we will apply the convention of using the sign of the parameter D_λ to describe the dispersion sign, as is usual in the field of optical fiber communications. Thus, the dispersion is compensated with 111 m of a positive dispersion fiber (Corning, model SMF28e+, with positive dispersion parameter D_λ), placed inside the laser cavity, and 22 m of a negative dispersion fiber (Thorlabs, model DCF38, with negative dispersion parameter D_λ), placed before the EDFA-C26. The source is schematized in Fig. 1, and more details can be found in ref. [5].

A measurement system is available for temporal characterization, based on collinear Frequency Resolved Optical Gating using Second Harmonic Generation (SHG-FROG). A Michelson autocorrelator performs the correlation between two replicas of the pulse, and makes them incident collinearly on a 300 μm BBO crystal (Beta-Barium Borate, CASTECH, Inc.). The SHG signal is spectrally resolved using a spectrometer (Qmini wideVIS spectrometer, RGB Photonics). Due to the interferometric interaction with the collinear configuration of the Michelson interferometer, the DC component has to be extracted from the interferometric traces in order to apply any of the known pulse retrieval algorithms [7,8]. Moreover, the optical spectrum from 1100 nm up to 1700 nm can be taken using an optical spectrum analyzer (OSA, Agilent, model 86142B).

To perform the measurements, the system has two output ports. The first output (O1) is located just before the HNLF. Due to the typical gain spectrum of erbium, in this output we can expect pulses with widths below 200 fs (reaching, at ideally, about 100 fs) and centered at 1560 nm. The second output (O2) is located after the HNLF. The temporal characterization at this point has required a substantial improvement in the measurement method (in essence, it is not easy to obtain enough intensity signal to generate SHG in the FROG setup). In this O2 output, we expect to obtain temporally compressed pulses with temporal widths of a few tens of fs, and with very broad spectra due to supercontinuum generation.

3. Simulations and optimization of the system

Before presenting the experimental results, we performed some numerical simulations of the pulse propagation within the HNLF in order to understand the physical phenomenon as well as to guide us in setting the system. The propagation of an ultrashort pulse through a nonlinear medium can be described using the generalized nonlinear Schrödinger equation [9] and for its simulation we have used the step-by-step method described by Dudley [10]. It is important to emphasize that the objective of these simulations is not to determine what exactly happens with the pulse, but to find evidences that tell us when the pulse
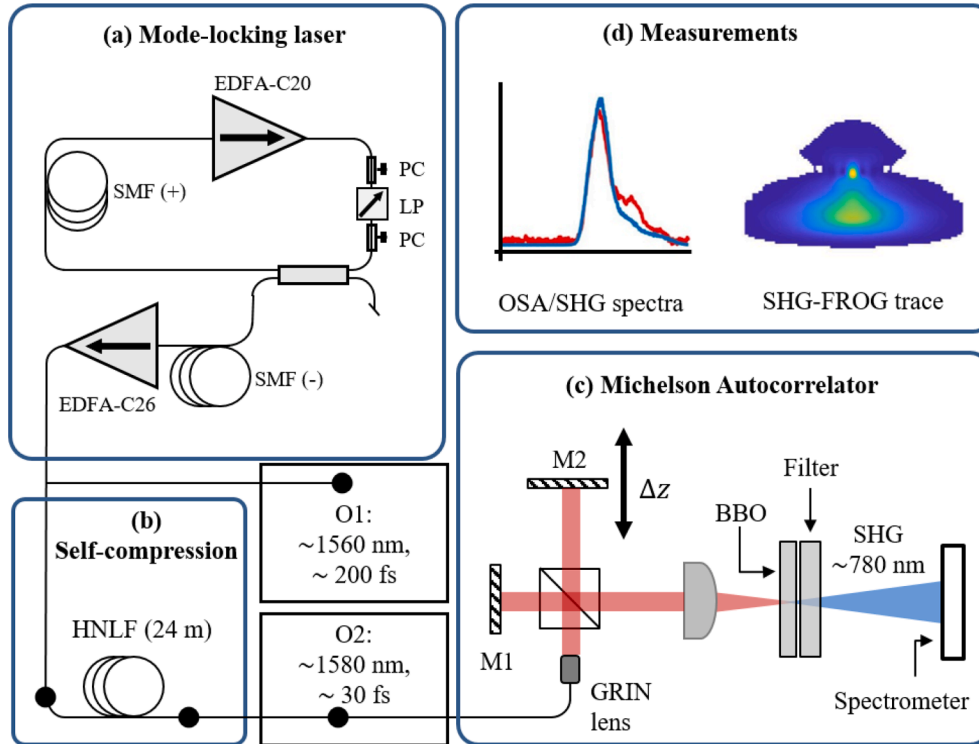

Fig. 1. Experimental set-up: (a) pulsed laser.
Source; (b) self-compression stage; (c) Michelson autocorrelator for characterization of the pulses; (d) examples of measurements. There are two output ports (one before and one after the HNLF, labelled as O1 and O2 respectively) where the pulses can be characterized

is successfully compressed, so that we can optimize the experimental setup. The reason for this is that we cannot be sure how much energy we are coupling into the HNLF, while also being unsure of how much of this energy is harnessed in the supercontinuum generation. Moreover, we do not have accurate and reliable data about the characteristics of the HNLF, and small variations in the dispersion curves produce noticeable effects on the simulations. Two parameters are normally used to assess whether the propagation is dominated by dispersive effects or by nonlinear effects. These parameters are the dispersive length and the nonlinear length, defined as,

$$L_D = \frac{T_0^2}{|\beta_2|}, L_{NL} = \frac{1}{\gamma P_0}, \tag{1}$$

where T_0 and P_0 are the width and the peak power of the seed pulse, β_2 is the second-order dispersion parameter and γ is the nonlinear parameter. We estimate the β_i values from ref. [6], obtaining $\beta_2 = -0.663 \text{ps}^2/\text{km}$, $\beta_3 = 0.0032 \text{ps}^3/\text{km}$ and $\beta_4 = -1 \bullet 10^{-4} \text{ps}^4/\text{km}$. In our case, since the dispersion value is very small while the peak power is very high, we have $L_{NL} < L_D$ and we can expect a behavior governed by nonlinear effects. On the other hand, the soliton order is defined as $N = \sqrt{\gamma P_0 L_D}$ (and therefore, $L_{NL} = L_D/N^2$). The numerical method of solving the equation requires a low soliton order to ensure that the approximations are valid [11], so in our case we limit it to $N = 8$. As we will see below, the pulses at the O1 output reach N values between 60 and 150. That is, we are assuming that the efficiency of the supercontinuum generation is below 10 %. We believe that this value may be reasonable, considering that we do not even control the polarization at the HNLF input, and that this value of N does not take into account the successive losses throughout the setup. We also assume a sech² shaped pulse as input pulse with a duration of 150 fs (Full Width Half-Maximum, FWHM). Thus, $L_{NL} = L_D/64$, consistent with the actual conditions. The propagation distance has been chosen so that the maximum compression position is within the simulation range (note that in the experiment, we can vary the input power, and therefore we can vary the maximum compression position). Fig. 2a shows the spectral evolution (in dB and normalized) and Fig. 2b collects the corresponding temporal evolution (linear scale and normalized to the maximum) in the range of L_{NL}. As can be seen, in the first stages of propagation (up to $11L_{NL}$) the pulse is temporarily compressed with the consequent spectral broadening. The maximum time compression occurs just where a Resonant Dispersive Wave (RDW) starts to be emitted (around a wavelength of 1200 nm in our simulation). Afterwards, the pulse loses its compactness, both in the spectral and time domains. The subsequent dynamics is usually explained in terms of soliton self-compression and fission [12], and a Raman soliton together with a RDW are clearly visible. As the pulse duration is reduced, its peak power is increased and it is able to generate the dispersive wave, broadening the spectrum and breaking the homogeneity of the pulse.

Therefore, we can use the emergence of the RDW as an indication of pulse compression.

To continue this analysis, and considering the experimental implementation, we set the propagation distance to achieve the maximum compression for a certain peak power P_0, and we simulate again several propagations varying this time the peak power (which is the parameter that we can modify experimentally by means of the C26 amplifier). Fig. 3a and b collect the output spectra and time evolution, respectively, for different peak powers from $0.60P_0$ up to P_0 (we choose these values in order to have similar results to those obtained experimentally). The relative height of each peak gives us an idea about the compression effect at each position with respect to the initial pulse. The labels in Fig. 3b indicate the temporal widths (FWHM) in each case. It is clear that the minimum width is obtained for the maximum peak power (dark blue line), but we can also note that the pulse is no longer compact. With this peak power, the dispersive wave (around 1186 nm) is clearly visible in the corresponding spectrum in Fig. 3a. When the RDW starts to be noticeable (red and yellow curves, for example), the pulse has been remarkably compressed maintaining a compact shape.

Therefore, optimizing the HNLF length until getting the appearance of a RDW may be a good indication of a correct configuration to achieve maximum temporal compression. Following this results, we tried to configure our setup as optimally as possible. Since the pumping current in the EDFA-C26 can be varied between 900 mA (threshold current) and 2700 mA, we try to optimize it at the middle of this range (around 1500 mA). First, we choose the SMF(−) and SMF(+) fiber lengths that maximize the signal at the BBO at O1 (resulting, as it was mentioned in Section 2, in 111 m of positive dispersion fiber inside de cavity and 22 m of negative dispersion fiber outside the cavity). We understand that this implies that the seed pulse dispersion has been sufficiently reduced, achieving the smallest possible duration. Next, we adjust the length of HNLF and we find that for 24 m (and pumping with 1500 mA) the spectrum reaches its maximum extension while the peak of the RDW is not visible yet. Fig. 3c collects different spectra at different currents (in logarithmic scale) with 24 m of HNLF. As we can see, the peak of this RDW (around 1219 nm) becomes clearly noticeable above 2100 mA. Thus, we can expect the maximum compression above 1800 mA. Besides the different spectral shape of the RDW, our measurements and our simulations differ significantly in the long wavelength region (around 1600 nm). It should be noted that the actual seed pulses introduced to the HNLF (whose spectra are shown in Fig. 3d are markedly different from the simulated pulses (dashed curve in Fig. 3d), particularly in this region of the spectrum. In any case, it should be remembered that we have used estimated values for the dispersion as well as for N, and that the objective of these simulations is only to illustrate the self-compression process in the HNLF. In the next section, we will show a complete calibration of our system, configured as we have explained here.
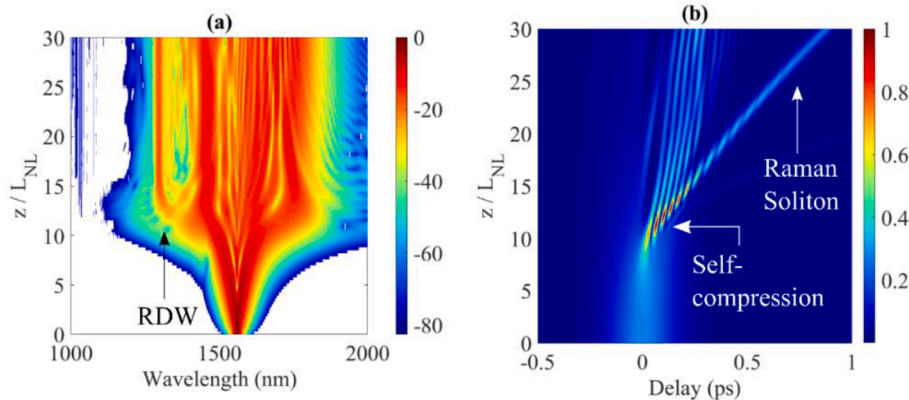

Fig. 2. Simulation of a 150 fs pulse travelling through the HNLF. The spectral and temporal evolution are plotted in (a) and (b), respectively.
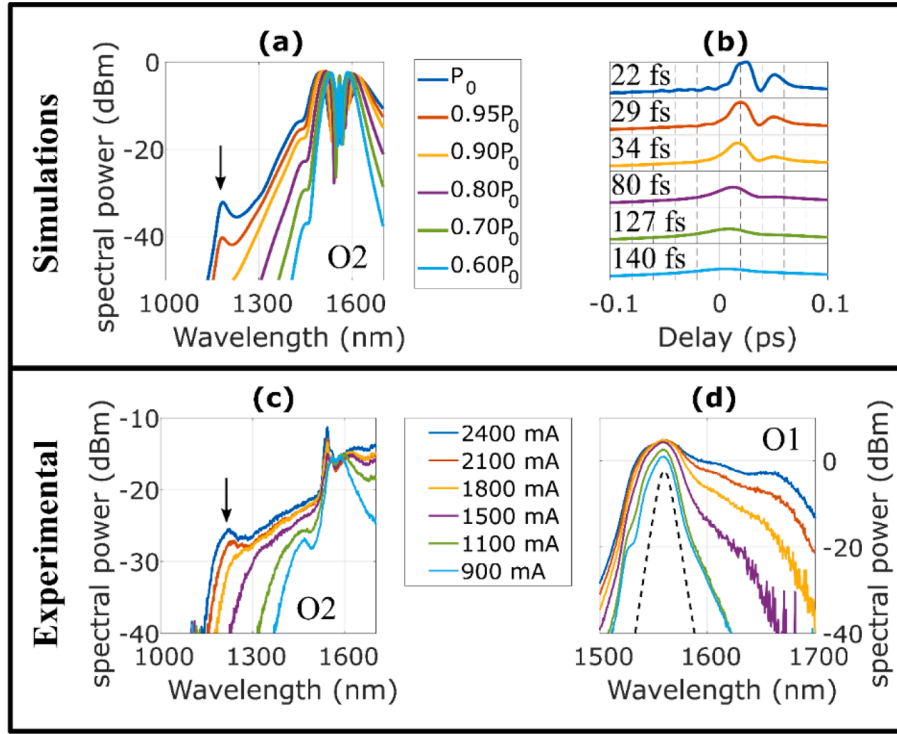
Fig. 3. Up: output spectra (a) and time evolution (b) at port O2 (simulated). Down: Measured spectra at output O2 (c) and O1 (d). The vertical arrows in (a) and (c) indicate the zones of RDW emission in each case. The dashed line in (d) shows the spectrum of a $sech^2$ shaped pulse.

4. Results

We can now assume that our installation is optimized, and proceed to its complete characterization. First, we characterize the pulses at the O1 output that will subsequently serve as seed for SC generation in the HNLF. Thus, we measure the spectral power using the OSA at O1 port for different amplifier pumping currents, shown in Fig. 4a (this time on a linear scale, for improved visibility). As can be seen, the spectral emission for low currents shows a central peak around 1560 nm. As the diode current increases, in addition to increasing the power at 1560 nm, the spectral region of higher wavelengths (lower frequencies) also rises, even reaching a second peak around 1655 nm. For the highest currents (above 2100 mA) the spectral density at the 1560 nm peak begins to decrease, just when the peak at 1655 nm is most noticeable. To better appreciate this behavior, Fig. 4b shows the spectral densities in the

1560 nm region (blue line) and in the 1655 nm region (orange line), using a 40 nm wide window. It seems clear that there is a change in behavior around 1800 mA. For completeness, we integrate the spectral curves to obtain the averaged power as a function of diode current, shown in the inset in Fig. 4b. As can be seen, we can obtain averaged powers from 5 mW up to 40 mW. This corresponds to soliton orders between 60 and 170, although we cannot be sure about the percentage of this power that is efficiently used in the generation of supercontinuum.

Our next step will be the temporal characterization at O1 port. Thus, we take interferometric FROG traces (iFROG), and extracting the DC component and subtracting the spectrum we obtain standard FROG traces [13]. Some of the traces obtained are shown in Fig. 5a. As can be seen, below 1800 mA the spectrum shows a very clear peak, and from 1800 mA a second lobe begins to appear at lower frequencies, which
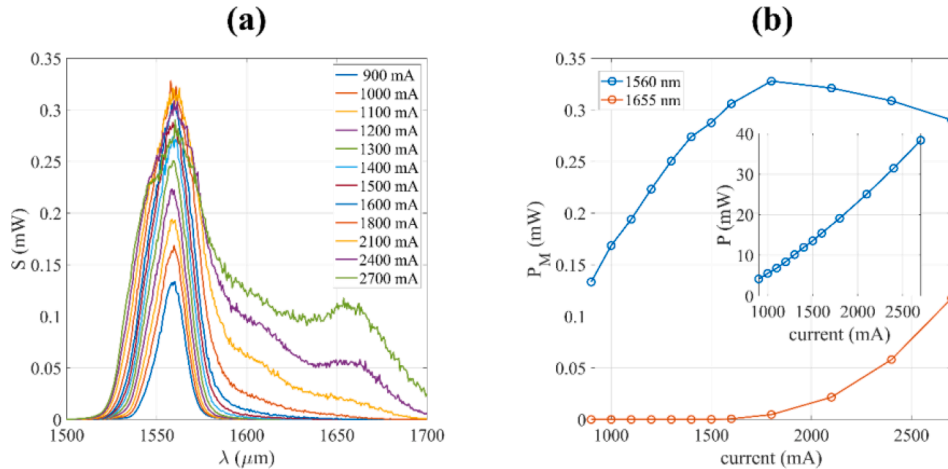

Fig. 4. Spectral power at Output O1; (a) OSA spectra (linear scale); (b) Maximum spectral power (P_M) in the windows 1540–1580 nm (labeled as 1560 nm) and 1635–1675 (labeled as 1655 nm) for different currents. The inset collects the spectral integration of the spectral densities (mean power, P).
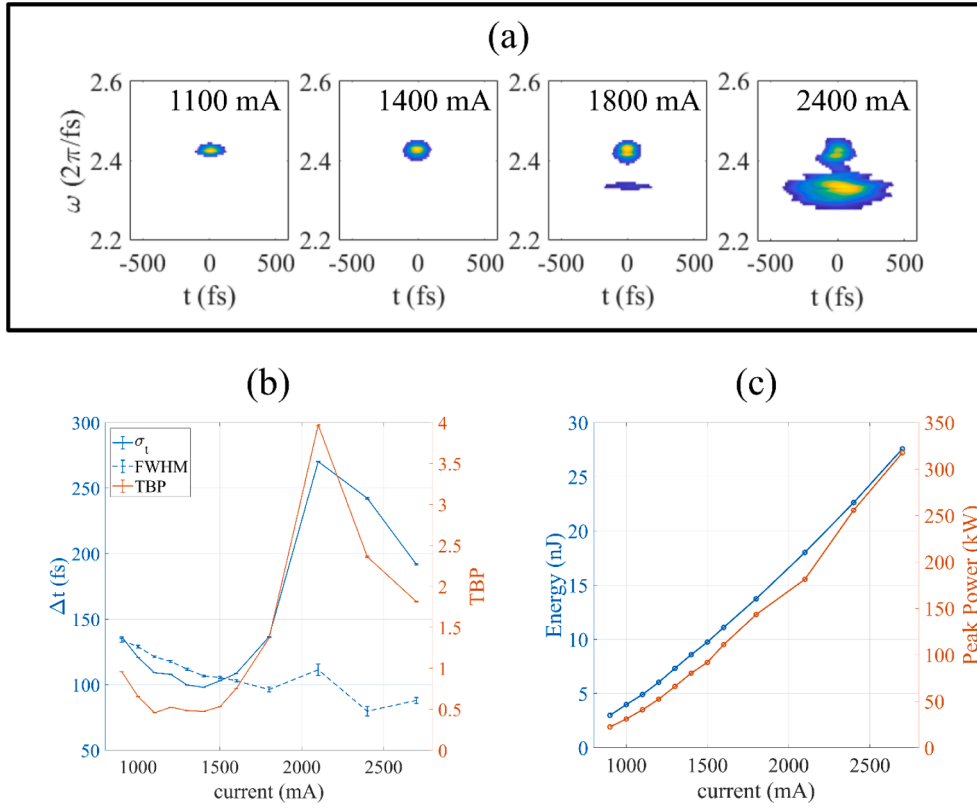
Fig. 5. Temporal characterization at Output O1; (a) FROG traces for different pumping currents; (b) Gaussian width (σ_t), FWHM and TBP of the retrieved pulses, averaged after 100 repetitions of the FROG algorithm with 200 iterations in each repetition; (c) Pulse energy and pulse peak power at output O1.

becomes even more powerful than the first peak when the pumping rises. These peaks correspond to the spectral curves shown in Fig. 4a and Fig. 4b, but it should be noted that the signal generated in the second harmonic also depends on the pulsed character of the electric field. We found that the FROG algorithm for pulse reconstruction achieves a satisfactory result in less than 200 iterations. However, the result depends on the pulse used as initial guess. For this reason, we make a series of 100 repetitions of the algorithm, using 200 iterations in each repetition, and beginning with a Gaussian pulse with random phase in each repetition. With the obtained retrievals, we calculate the average FWHM, shown in Fig. 5b. The widths obtained are of the order of 100 fs, showing a decrease in temporal width with the diode current in accordance with the spectral broadening seen above.

In order to perform a more exhaustive analysis, we also calculate the time-bandwidth product (*TBP*). Usually this calculation is done by using the intensity FWHM and estimating a deconvolution factor assuming a type of pulse profile (for example, sech^2 or Gaussian shape). This calculation is not valid for pulses with a more complex structure [14], so we prefer to use second order moments. Knowing that the variance of a Gaussian distribution is the squared Gaussian width, we can calculate the temporal and spectral widths of the field distributions (denoted as σ_t and σ_ν) as follows,

$$\sigma_t = 2\sqrt{Var(I(t))} = 2\sqrt{\int (t-t_0)^2 I(t)dt},$$

$$\sigma_\nu = 2\sqrt{Var(I(\nu))} = 2\sqrt{\int (\nu-\nu_0)^2 I(\nu)d\nu}. \qquad (2)$$

Note that in this definition we have used $I(t)$ and $I(\nu)$ (the intensity distributions in the time and frequency domain respectively). Parameters t_0 and ν_0 can be understood as the center of mass of the intensity distributions. The value of σ_t for each current is also plotted in Fig. 5b.

We can see that σ_t and FWHM are decreasing up to a certain value, around 1600 mA. Above this current, FWHM continues to decrease, while σ_t increases significantly. We interpret this result as an evidence that it is not appropriate to use the FWHM parameter in these cases, since the pulses are no longer compact, while σ_t does show an appropriate value of the Gaussian distribution of the intensity. Thus, the time-bandwidth product *TBP* is simply defined as,

$$TBP = \sigma_t \sigma_\nu. \qquad (3)$$

With this definition, the *TBP* reaches a minimum value around 0.32 for a Gaussian pulse with planar instantaneous frequency, and higher values of *TBP* indicate pulses with time-dependent instantaneous frequency. Note also that the minimum value of *TBP* can be different for other pulse shapes [14]. For example, for hyperbolic secant shaped pulses the minimum value is 0.41. Fig. 5b also shows the evolution of *TBP* with the diode current. It can be seen that the pulses are optimized for currents between 1100 mA and 1500 mA, with *TBP* values below 0.5. A minimum value of *TBP* = 0.45 is obtained for 1100 mA (close to the minimum value for hyperbolic secant shaped pulses). Above 1600 mA, the *TBP* value grows notably, indicating that the pulses are no longer Gaussian or hyperbolic secant shaped pulses (as can also be seen in the spectra shown in Fig. 4a). In addition, we integrate the spectral densities in Fig. 4a to obtain the averaged power. Then, using the repetition rate and the estimated time duration of the pulses we can compute the Energy per pulse and the pulse Peak Power, shown in Fig. 5c. As might be expected, these variables increase as the current grows.

Next, we move on to characterize the pulses at the O2 output. Fig. 6 shows some of the FROG traces obtained for different pumping currents. The first thing that is remarkable in these measurements is the temporal narrowing of the interferometric traces as the pumping current grows. To see this better, we also show the interferometric autocorrelation (IAC) traces together with the FWHM of these traces. We see that the estimated durations have fallen below 100 fs. This should correspond to
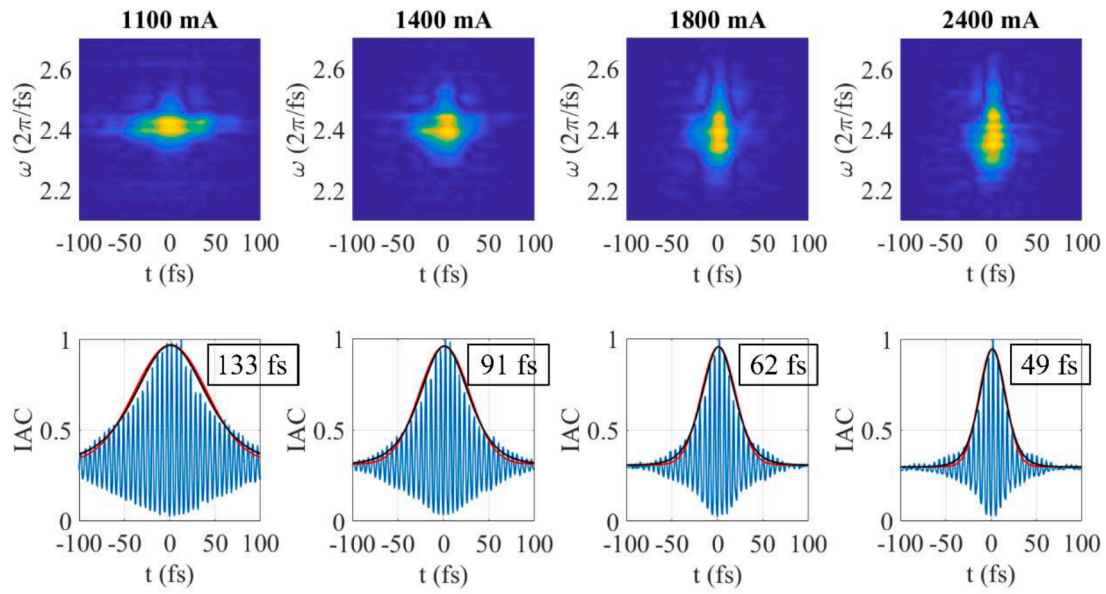
Fig. 6. FROG traces (up) and corresponding interferometric autocorrelation traces (down) for different driving currents at output O2. Red and black curves correspond to Gaussian and sech^2 profiles, respectively, fitted to interferometric trace envelopes. (For interpretation of the references to colour in this figure legend, the reader is referred to the web version of this article.)

a spectral broadening, also clearly noticeable in the FROG traces. We also see that the appearance of the autocorrelations is quite compact, and no lobes or satellite pulses are visible. However, fitting to a Gaussian profile (red curves in Fig. 6), we observe that the IAC traces for high currents show a slight pedestal that worsens slightly the Gaussian fitting. This indicates that the pulses will have, in addition to a central peak with
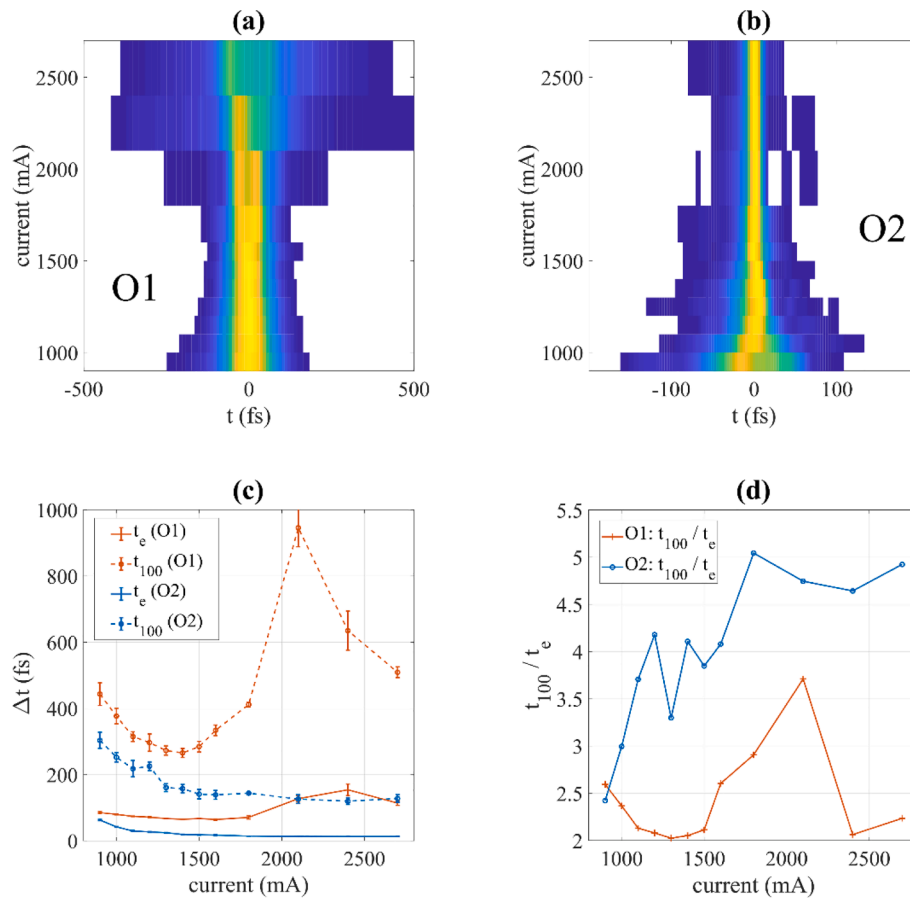

Fig. 7. Temporal characteristics of the retrieved pulses at outputs O1 and O2 for different currents. Up: Averaged intensities in time domain, at output O1 (a) and O2 (b). Only intensities above $I_{MAX}/100$ for each current are plotted. Down: temporal widths at $I_{MAX}/100$ are collected in (c) for O1 and O2. The averaged pedestal factor, t_{100}/t_e are plotted in (d).

durations of tens of femtoseconds, a pedestal with a low relative power.

It is also common to fit the trace envelopes to a sech^2 profile, also shown in Fig. 6 (black lines). Although the traces seem to fit the sech2 profiles a bit better, both fits are very similar and the pedestal is still visible. Thus, we prefer not to make any assumptions about the pulse shape, and will henceforth use the fits to Gaussian profiles.

To study the importance of these pedestals, we define new variables describing the pulse duration. The quantity t_i indicates the temporal full width of the pulse when its intensity falls to $1/i$ of the maximum intensity. Thus, for example, t_e corresponds to $2\sigma_t$, since we are using the full width (not the half-width) of the intensity at a height $1/e$ of the maximum. Averaging the 100 repetitions of the FROG algorithm, we show in Fig. 7a and Fig. 7b the evolution of the pulses as a function of the diode currents. These figures have been truncated to a value $1/100$ of the maximum. Although this value is very restrictive, we understand that by averaging over 100 pulses we are filtering out small variations. Nevertheless, it can be seen that the pulses show a clear central pulse in all cases. At the O1 output (Fig. 7a) the pedestal becomes minimal between 1500 or 1800 mA, and grows enormously above 1800 mA. This is consistent with the appearance of a second peak in the spectrum. On the contrary, we see that, at the O2 output (Fig. 7), the pedestal width always decreases as the diode current increases, although this decrease seems to stagnate around a minimum value (around 20 fs time-width).

To see this in more detail, and also to analyze the shape of the pulses, we compare t_{100} and t_e widths at both outputs (Fig. 7c). The blue lines show the Gaussian widths at both outputs, and the compression effect achieved at the O2 output can be clearly observed. It can also be seen that from 1800 mA onwards the pulse is no longer compact at output O1, contrary to what happens at output O2. Something similar can be said about the t_{100} widths (orange lines). To see the compression effect achieved, Fig. 7d shows the ratio t_{100}/t_e for each output. This factor can be understood as a measure of the quality of the pulse in terms of compactness. As we can see, the curve for output O1 shows a strange behavior above 1600 mA, which we must again explain by the fact that the pulse is no longer compact. Below this current, the width t_{100} is only about twice as large as the width t_e. In contrast, the blue curve shows this compactness factor for the O2 output. As can be seen, this ratio reaches values close to 5 for high currents, showing that the pulse is much more compact at the O2 output (which also indicates that FWHM can be used to measure the temporal width of the pulses at O2). The best compactness value has been obtained for 1800 mA, coinciding with our assumption in the system optimization.

5. Discussion

At this point, we are ready to study the compression capability of the HNLF fiber. Fig. 8a shows the time-widths of the pulses at the O2 output. As we have already seen that the pulses at this output are compact, we use the FWHM to measure the temporal width, since this is the most common parameter in the literature. As we can see, the width is always below 100 fs, stabilizing at widths less than 20 fs (the smallest width reached is 17 fs). On the other hand, Fig. 8a also shows the compression factor, defined as the ratio between the widths at outputs O1 and O2. We see that the pulses become up to six times shorter, due to the presence of the HNLF fiber.

In addition, Fig. 8b shows the TBP of the pulses at the O2 output. We see that in this case the TBP stabilizes at values close to 0.8, reaching a minimum of 0.76 for 1400 mA. That is, a value twice that of a Fourier-limited pulse. This indicates that the pulses achieved at the output O2 still have room for improvement, if some other methods of phase compensation were used (such as adding dispersion-controlled fibers).

Finally, Fig. 9 shows three of the retrieved pulses at the O2 output (it should be reminded that the SHG-FROG technique presents an ambiguity in the time direction). We have chosen the three most representative pulses: the one with the lowest TBP (obtained for 1400 mA, 24 fs time-width), the one with the lowest t_{100}/t_e ratio (obtained for 1800 mA, 19 fs time-width), and the one with the lowest FWHM (obtained for 2700 mA, 17 fs time-width). It can be seen that that there is enough agreement in the retrieved phases. It is also noted that the pulses are quite compact and their temporal phases are reasonably flat, while the satellite pulses have a rather small relative amplitude in all three cases (note that the black line, obtained by averaging all the reconstructions, tends to filter out the satellites).

To put our results in context, Table 1 shows some FWHM reported by other authors employing similar setups. We have limited our search to pulses produced with erbium-doped fiber ring-lasers, and compressed using HNLF (either in combination with other elements or without the use of any other component). As we can see, our pulses have a FWHM practically equal to the narrowest pulses reported with these techniques [16,20]. In general, it is easy to find pulses below 30 fs, but not so easy to find pulses with durations below 20 fs. This fact can be attributed to the pulsed frequency of our source, which is notably lower than the frequencies used by other more common sources. This allows us to achieve much higher energy and peak power (being easier to generate non-linear effects), since it is very easy to vary this frequency in ring lasers by simply increasing the length of the cavity (in our case, this was done to control the dispersion of the pulses inside the cavity). On the other hand, we see that the few papers that present slightly better results than ours
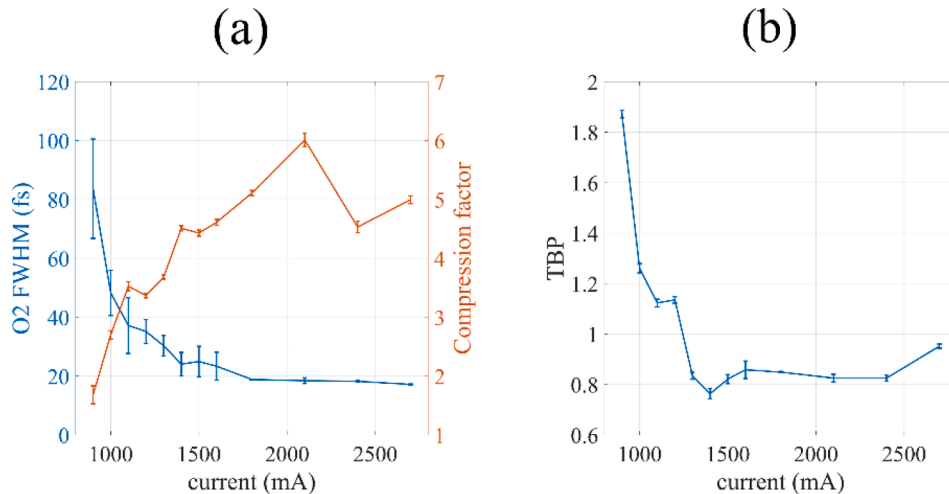

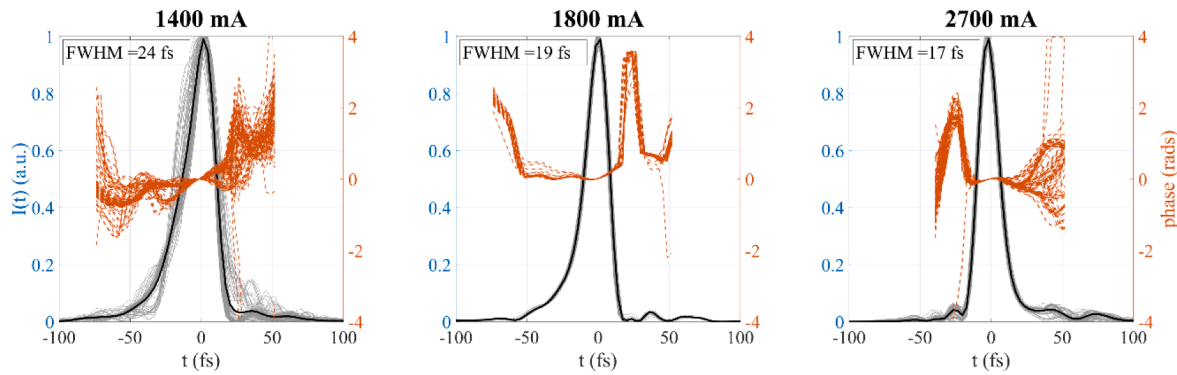**Fig. 8.** Temporal behavior at output O2 (a), and TBP at output O2 (b).

Fig. 9. Retrieved compressed pulses at output O2 for different cases: best TBP (1400 mA), best compactness factor (1800 mA) and shortest duration (2700 mA). Left axis: intensity (gray lines correspond to the 100 retrieved pulses in each case, black lines show the averaged intensity values of the retrieved pulses). Right axis: phase in radians (dashed lines).

Table 1
FWHM reported by other authors.

Seed				Compressed		Ref
Δt(fs)	Freq. (MHz)	E_P(nJ)	P_P(kW)	Minimum Δt (fs)	Compressor and Dispersion control	
224	45.5	2.66	11.875	24	SMF No dispersion control	[15]
110	40	3.52	32	15.9	Anomalous dispersion + normal PMF	[16]
110	40	3.63	33	22.9	Anomalous dispersion PM + HNLF	[17]
100	35	1.5	15	22	SMF + HNLF	[18]
1000	44.6	3.07	< 1	22.7	SMF No dispersion control	[19]
25	45	2.6	104	16.5 (Subpulses)	PM_HNLF No dispersion control	[20]
100	1.4	5–30	30–300	17	HNLF No dispersion control	This work

need to optimize the pulses after compression, or need to use polarization-maintaining fiber. In our case, we do not need to add more elements to our setup, thus achieving a much simpler system. Moreover, our pulses still present room for improvement (particularly by reducing the TBP), so we can expect an improvement in these results in the future.

6. Conclusions

In summary, we have shown an EDFA-ring laser with sub-20 fs pulses around 1560 nm. For this purpose, we have used non-linear effects in a HNLF. Through simulations and experimental measurements we have found that the emission of a RDW is a good indicator of the point of maximum compression. At the same time, we have optimized the pulses at the input of the HNLF by maximizing the signal generated in a BBO. Therefore, we have succeeded in compressing our pulses to the level of the best published results. Moreover, we have achieved it by using a much simpler system (only one step to reduce the duration below 20 fs). The smallest time-widths achieved are 17 fs. A comparison with other similar works shows us that it is relatively common to obtain pulses slightly longer than 20 fs, but it is much more difficult to obtain pulses of widths smaller than 20 fs. In fact, the works that achieve widths similar to ours use much more complicated setups. The simplicity of our setup, together with the good results we have achieved, indicates that further investigation of this pulse compression strategy is appropriate.

Furthermore, the TBP indicates that there is still room for improvement, leaving the way open for further advances in the near future.

CRediT authorship contribution statement

Francisco Javier Salgado-Remacha: Writing – original draft, Investigation, Conceptualization. **Sebastián Jarabo:** Writing – review & editing, Investigation, Conceptualization.

Declaration of competing interest

The authors declare that they have no known competing financial interests or personal relationships that could have appeared to influence the work reported in this paper.

Data availability

Data will be made available on request.

References

[1] Y. Han, Y. Guo, B.o. Gao, C. Ma, R. Zhang, H. Zhang, Generation, optimization, and application of ultrashort femtosecond pulse in mode-locked fiber lasers, Prog. Quantum Electron. 71 (2020) 100264, https://doi.org/10.1016/j.pquantelec.2020.100264.
[2] J.M. Dudley, G. Genty, S. Coen, Supercontinuum generation in photonic crystal fiber, Rev. Mod. Phys. 78 (4) (2006) 1135–1184, https://doi.org/10.1103/RevModPhys.78.1135.
[3] C. Li, X. Wei, C. Kong, S. Tan, N. Chen, J. Kang, K.K.Y. Wong, Fiber chirped pulse amplification of a short wavelength mode-locked thulium-doped fiber laser, APL Photonics 2 (12) (2017) 121302, https://doi.org/10.1063/1.4996441.
[4] D.G. Purdie, D. Popa, V.J. Wittwer, Z. Jiang, G. Bonacchini, F. Torrisi, S. Milana, E. Lidorikis, A.C. Ferrari, Few-cycle pulses from a graphene mode-locked all fiber laser, Appl. Phys. Lett. 106 (25) (2015) 253101, https://doi.org/10.1063/1.4922397.
[5] J.E. Saldaña-Díaz, S. Jarabo, F.J. Salgado-Remacha, Supercontinuum source based on all-silica fibers with optimized spectral power from 1100 up to 2300 nm, Opt. Laser Technol. 117 (2019) 73–78, https://doi.org/10.1016/j.optlastec.2019.04.011.
[6] Yangtze Optical Fibre and Cable Company Ltd., NL-1550-Zero, https://en.yofc.com/view/2353.html.
[7] N.C. Geib, M. Zilk, T. Pertsch, F. Eilenberger, Common pulse retrieval algorithm: a fast and universal method to retrieve ultrashort pulses, Optica 6 (4) (2019) 495–505, https://doi.org/10.1364/OPTICA.6.000495.
[8] M. López-Ripa, B. Alonso, S. Jarabo, F.J. Salgado-Remacha, J.C. Aguado, Í.J. Sola, Coherent artifact and time-dependent polarization in amplified ultrafast erbium-

doped fibre lasers, Opt. Laser Technol. 140 (2021) 107018, https://doi.org/10.1016/j.optlastec.2021.107018.

[9] G.P. Agrawal, Nonlinear Fiber Optics, 4th ed., Academic Press, 2007.

[10] J. Dudley, J. Taylor (Eds.), Supercontinuum Generation in Optical Fibers, Cambridge University Press, Cambridge, 2010, https://doi.org/10.1017/CBO9780511750465.

[11] S. Roy, S.K. Bhadra, G.P. Agrawal, Dispersive waves emitted by solitons perturbed by third-order dispersion inside optical fibers, Phys. Rev. A 79 (2) (2009) 0.23824, https://doi.org/10.1103/PhysRevA.79.023824.

[12] C. Brahms, J.C. Travers, Soliton self-compression and resonant dispersive wave emission in higher-order modes of a hollow capillary fibre, Journal of Physics: Photonics 4 (3) (2022) 034002, https://doi.org/10.1088/2515-7647/ac6345.

[13] G. Stibenz, G. Steinmeyer, Interferometric frequency-resolved optical gating, Opt. Express 13 (7) (2005) 2617–2626, https://doi.org/10.1364/OPEX.13.002617.

[14] M. Wollenhaupt, A. Assion, T. Baumert, in: Femtosecond Laser Pulses: Linear Properties, Manipulation, Generation and Measurement, Springer Handbook of Lasers and Optics. Springer, New York, NY, 2007, https://doi.org/10.1007/978-0-387-30420-5_12.

[15] J. Sotor, G. Sobon, 24 fs and 3 nJ pulse generation from a simple, all polarization maintaining Er-doped fiber laser, Laser Phys. Lett. 13 (12) (2016) 125102, https://doi.org/10.1088/1612-2011/13/12/125102.

[16] B. Sierro, P. Hänzi, D. Spangenberg, A. Rampur, A.M. Heidt, Reducing the noise of fiber supercontinuum sources to its limits by exploiting cascaded soliton and wave breaking nonlinear dynamics, Optica 9 (4) (2022) 352–359, https://doi.org/10.1364/OPTICA.450505.

[17] P. Hänzi, B. Sierro, Z. Liu, V. Romano, A. Rampur, A.M. Heidt, Benefits of cascaded nonlinear dynamics in hybrid fibers for low-noise supercontinuum generation, Opt. Express 31 (7) (2023) 11067–11079, https://doi.org/10.1364/OE.481970.

[18] B. Kibler, U.C. Fischer, P.A. Lacourt, F. Courvoisier, R. Ferriere, L. Larger, D.N. Neshev, J.M. Dudley, Optimized one-step compression of femtosecond fibre laser soliton pulses around 1550 nm to below 30 fs in highly nonlinear fibre, Electron. Lett 43 (17) (2007) 915–916, https://doi.org/10.1049/el:20071726.

[19] H. Luo, L. Zhan, L. Zhang, Z. Wang, C. Gao, X. Fang, Generation of 22.7-fs 2.8-nJ Pulses From an Erbium-Doped All-Fiber Laser Via Single-Stage Soliton Compression, J. Lightwave Technol. 35 (17) (2017) 3780–3784, https://doi.org/10.1109/JLT.2017.2723088.

[20] K. Tarnowski, T. Martynkien, P. Mergo, J. Sotor, G. Soboń, Compact all-fiber source of coherent linearly polarized octave-spanning supercontinuum based on normal dispersion silica fiber, Sci. Rep. 9 (2019) 12313, https://doi.org/10.1038/s41598-019-48726-9.